

RESEARCH

Open Access



Prognostic model for predicting Alzheimer's disease conversion using functional connectome manifolds

Sunghun Kim^{1,2}, Mansu Kim³, Jong-eun Lee^{1,2}, Bo-yong Park^{2,4*} and Hyunjin Park^{2,5*}

Abstract

Background Early detection of Alzheimer's disease (AD) is essential for timely management and consideration of therapeutic options; therefore, detecting the risk of conversion from mild cognitive impairment (MCI) to AD is crucial during neurodegenerative progression. Existing neuroimaging studies have mostly focused on group differences between individuals with MCI (or AD) and cognitively normal (CN), discarding the temporal information of conversion time. Here, we aimed to develop a prognostic model for AD conversion using functional connectivity (FC) and Cox regression suitable for conversion event modeling.

Methods We developed a prognostic model using a large-scale Alzheimer's Disease Neuroimaging Initiative dataset, and it was validated using external data obtained from the Open Access Series of Imaging Studies. We considered individuals who were initially CN or had MCI but progressed to AD and those with MCI with no progression to AD during the five-year follow-up period. As the exact conversion time to AD is unknown, we inferred this information using imputation approaches. We generated cortex-wide principal FC gradients using manifold learning techniques and computed subcortical-weighted manifold degrees from baseline functional magnetic resonance imaging data. A penalized Cox regression model with an elastic net penalty was adopted to define a risk score predicting the risk of conversion to AD, using FC gradients and clinical factors as regressors.

Results Our prognostic model predicted the conversion risk and confirmed the role of imaging-derived manifolds in the conversion risk. The brain regions that largely contributed to predicting AD conversion were the heteromodal association and visual cortices, as well as the caudate and hippocampus. Our risk score based on Cox regression was consistent with the expected disease trajectories and correlated with positron emission tomography tracer uptake and symptom severity, reinforcing its clinical usefulness. Our findings were validated using an independent dataset. The cross-sectional application of our model showed a higher risk for AD than that for MCI, which correlated with symptom severity scores in the validation dataset.

Conclusion We proposed a prognostic model predicting the risk of conversion to AD. The associated risk score may provide insights for early intervention in individuals at risk of AD conversion.

Keywords Alzheimer's disease, Disease conversion, Functional connectivity, Gradient, Cox regression

*Correspondence:

Bo-yong Park
boyongpark@korea.ac.kr
Hyunjin Park
hyunjinp@skku.edu

Full list of author information is available at the end of the article



© The Author(s) 2024. **Open Access** This article is licensed under a Creative Commons Attribution-NonCommercial-NoDerivatives 4.0 International License, which permits any non-commercial use, sharing, distribution and reproduction in any medium or format, as long as you give appropriate credit to the original author(s) and the source, provide a link to the Creative Commons licence, and indicate if you modified the licensed material. You do not have permission under this licence to share adapted material derived from this article or parts of it. The images or other third party material in this article are included in the article's Creative Commons licence, unless indicated otherwise in a credit line to the material. If material is not included in the article's Creative Commons licence and your intended use is not permitted by statutory regulation or exceeds the permitted use, you will need to obtain permission directly from the copyright holder. To view a copy of this licence, visit <http://creativecommons.org/licenses/by-nc-nd/4.0/>.

Background

Alzheimer's disease (AD) is a fatal neurodegenerative disease that affects memory and disrupts cognitive and bodily functions [1]. The neurodegenerative process begins before the clinical symptoms of AD are evident and is likely to progress through mild cognitive impairment (MCI) [2]. Conversion from MCI to AD is a pressing concern, with almost 80% of patients with MCI converting to AD over six years [3]. Despite the significant global health implications of AD [4], curative treatments remain elusive, highlighting the need for developing reliable biomarkers to assess the risk of conversion to AD.

Neuroimaging studies have been widely conducted to identify imaging markers that provide early indications of AD onset [5–10]. It has been shown that early AD manifestations were linked to functional abnormalities in the hippocampus and cortical atrophy in the memory-related network [11–13], notably the default mode network, which has been found to have decreased metabolism in the early stages of AD [14]. In addition, cortical thinning in the posterior cingulate and inferior parietal regions [15], and reductions in the subcortical volumes of the hippocampus, amygdala, thalamus, and putamen becoming more pronounced over time correlate with cognitive impairment [16, 17]. Studies using resting-state functional magnetic resonance imaging (rs-fMRI) have found decreased functional connectivity (FC) in the default mode network of patients with AD [18–20]. In particular, changes in FC between the hippocampi in the medial temporal lobes and posterior cingulate cortex indicate early neurodegeneration in individuals susceptible to AD [21, 22]. The previous work suggested that vascular dysregulation plays a key role in the early stages of the disease, subsequently leading to amyloid- β deposition, metabolic dysfunction, functional impairment, and structural atrophy [10]. Although fMRI measures the consequences of molecular-level alterations, it is a powerful imaging modality that can assess functional brain organization by assessing inherently changing functional dynamics of the brain in vivo. These findings underscore the feasibility of using FC as a tool for identifying early AD biomarkers.

Despite extensive research, most studies have primarily focused on the differences between individuals with MCI (or AD) and cognitively normal (CN) individuals [23, 24] or the differences between AD converters and non-converters, typically involving group-level comparisons at either baseline or follow-up imaging evaluations [25, 26]. These studies are important for understanding the differences between AD and CN but lack evidence of time-related changes in brain dynamics during disease progression. For example, the current approach to comparing AD converters and non-converters tends to

overlook temporal information, such as varying conversion times (e.g., three years vs. five years). Furthermore, these approaches often do not consider right-censored data, which is common in longitudinal studies. Therefore, a more comprehensive understanding of the temporal aspects of patient conversion from MCI (or CN) to AD is required.

Recently, connectome gradient approaches have been proposed to capture the functional organization of the human brain [27, 28]. This technique quantifies gradual transitions in connectivity and provides comprehensive hierarchical information about the brain by projecting high-dimensional connectivity data onto a low-dimensional manifold space. The principal gradient expands from the transmodal to the unimodal areas, whereas the second gradient differentiates between the visual and somatomotor cortices. Furthermore, subcortico-cortical functional interactions have been explored by situating changes in subcortico-cortical pathways in the macroscale context of cortico-cortical connectivity [29, 30]. It has been shown that AD is a disease involving hierarchical brain disorganization [31]. Thus, we hypothesized that the gradient techniques applied to fMRI data, besides perfusion imaging, could identify changes in the functional brain hierarchy of individuals at risk of conversion to AD, helping early diagnosis of AD.

Here, we developed a prognosis model that considers AD conversion. We established the role of macroscale FC gradients in individuals at risk of conversion to AD before the progression occurred using baseline rs-fMRI data. By identifying these early biomarkers, we aimed to develop robust predictive models for AD risk, which could allow timely interventions, potentially slowing disease progression. Our comprehensive analysis included whole-brain FC with vulnerability to functional alterations linked to AD conversion. We used large-scale AD data containing both baseline and follow-up data obtained from the Alzheimer's Disease Neuroimaging Initiative (ADNI) [32] and validated the findings in an independent dataset from the Open Access Series of Imaging Studies (OASIS) database [33].

Methods

Study participants

i) ADNI dataset

Imaging and phenotypic data were obtained from the ADNI database (<https://adni.loni.usc.edu/>) [32]. ADNI was launched in 2003 as a public-private partnership led by principal investigator Michael W. Weiner. The primary goal of the ADNI is to test whether serial MRI, positron emission tomography (PET), other biological markers, and clinical and neuropsychological assessments can be combined to measure the progression of MCI and early

AD. In the ADNI database, we considered participants who were initially categorized as CN or as having MCI but progressed to AD and censored individuals who did not convert to AD. We applied the following criteria to select participants at risk of progression to AD: (1) availability of multimodal imaging dataset (i.e., T1-weighted [T1w], rs-fMRI) with sufficient image quality (i.e., 3 T), (2) head motion with mean framewise displacement < 0.3 mm, and (3) participants diagnosed with AD within five years of the scan date (CN or MCI \rightarrow AD) and individuals diagnosed as CN or with MCI during the five-year follow-up period (CN \rightarrow MCI or MCI \rightarrow MCI, thus right-censored) and (4) excluded reversion cases (e.g., AD \rightarrow MCI). The five-year limit of time to conversion was imposed so that the baseline MRI data might possess prognostic power for the conversion event that occurred later, as previously reported [34, 35]. This resulted in the selection of 68 unique participants from the ADNI-GO/2/3 datasets who were at risk of conversion to AD. Due to the limited number of unique participants, we included one session from the study participants that revisited the study (e.g., 6 or 12 months), constituting a total dataset of 115 samples. The sample consisted of participants who were CN or with MCI (mean age, 72.9 years; 51% male), and the median conversion time from baseline to AD was 1,277 days, with a 48% conversion rate. In summary, each sample had a baseline scan and an associated conversion date; however, some samples were obtained from the same participant. We considered demographic and clinical variables, including age, sex, Mini-Mental State Examination (MMSE) score, apolipoprotein E4 (APOE4) status, and education level, as these factors are known to contribute to the complex etiology of AD. The discovery dataset was defined as the *ADNI risk dataset*, and the demographic information of the 115 samples is detailed in Supplementary Table 1.

ii) OASIS dataset

To validate our model, we constructed two external validation datasets from the OASIS3 database: the *OASIS risk dataset* and the *OASIS diagnosis dataset*. To construct the *OASIS risk dataset*, we adopted the same participant selection process as that used in the *ADNI risk dataset*. The *OASIS risk dataset* consisted of 33 unique participants curated to reflect the characteristics of the *ADNI risk dataset*. In addition, the *OASIS diagnosis dataset* included 803 unique participants, each labeled with their respective diagnoses. More details on these datasets are provided in Supplementary Table 2 and Supplementary Table 3, respectively. Institutional Review Board (IRB) approvals were obtained from the original study depicting the ADNI and OASIS databases. In the ADNI dataset, consent forms were approved by each

participating site's IRB. The IRB of Washington University School of Medicine approved the OASIS study and written informed consent was obtained for all participants. All ADNI and OASIS datasets have been fully anonymized, with no protected health information included.

Data acquisition

i) MRI data

Imaging data were acquired using 3 T GE, Philips, and Siemens scanners. In ADNI-GO/2 phases, T1w images were obtained using a 3D magnetization-prepared rapid acquisition gradient echo (MPRAGE) sequence (repetition time [TR]=6.8 ms; echo time [TE]=3.2 ms, flip angle=9°). The rs-fMRI data were acquired using a 2D echo planar imaging (EPI) sequence (TR=3,000 ms; TE=30 ms; flip angle=80°; number of volumes=140, and voxel size=3.31 \times 3.31 \times 3.31 mm³). In ADNI-3 phase, T1w images were obtained using a 3D MPRAGE sequence (TR=2,300 ms; TE=2.98 ms; flip angle=9°), and rs-fMRI data were acquired using an EPI sequence (TR=3,000 ms; TE=30 ms; flip angle=90°; number of volumes=197; and voxel size=3.4 \times 3.4 \times 3.4 mm³). Imaging data in OASIS3 were acquired using Siemens TIM Trio 3 Tesla scanners. T1w images were obtained using a 3D MPRAGE sequence (TR=2.4 ms; TE=3.2 ms; flip angle=8°), and the rs-fMRI data were acquired using a 2D EPI sequence (TR=2,200 ms; TE=27 ms; flip angle=90°; number of volumes=164, and voxel size=4 \times 4 \times 4 mm³).

ii) PET data

For PET images from ADNI-GO/2/3, standardized dynamic protocols were applied. The amyloid- β PET consisted of AV45- and FBB-PET. For AV45-PET, a protocol lasting 50–70 min post-intravenous injection of 370 MBq of [¹⁸F] Florbetapir was used, with a scan duration of 20 min divided into four 5-min frames. For FBB-PET, the protocol lasted 90–110 min post-intravenous injection of 300 MBq of [¹⁸F] Florbetaben, with a 20-min scan divided into four 5-min frames. For FDG-PET, a 30–60 min protocol post-injection of 185 MBq of [¹⁸F] Fludeoxyglucose was used, with a 30-min scan divided into six 5-min frames. For Tau-PET, a 75–105 min protocol post-injection of 370 MBq of [¹⁸F] AV-1451 (Flortaucipir) was applied, with a 30-min scan divided into six 5-min frames. All PET data we employed were from baseline tracer scores matched to the baseline fMRI sessions. In the PET tracer comparison, only baseline session PET data were used. If PET data were unavailable due to missing modality, they were excluded from the PET tracer score analyses.

Data preprocessing

i) MRI data

MRI data preprocessing of the ADNI and OASIS data was performed using fMRIPrep [36]. T1w images were corrected for intensity non-uniformity. A T1w-reference map was computed after the registration of multiple T1w images, and the skull was removed. Brain tissue segmentation of the cerebrospinal fluid, white matter, and gray matter was performed on the brain-extracted T1w images using FSL. Volume-based spatial normalization to the standard MNI152 space was performed through nonlinear registration using ANTs [37]. Brain surfaces were reconstructed using FreeSurfer [38]. For each rs-fMRI session, slice timing was adjusted, and the head motion was corrected by registering the volume of each time point to the reference volume of the middle time point. The reference time-point data were coregistered to the T1w-reference image using boundary-based registration and then registered onto the MNI152 template. Spatial smoothing with an isotropic Gaussian kernel of 6 mm full-width half-maximum (FWHM) was applied, and removal of residual motion artifacts was performed using independent component analysis-based automatic removal of motion artifacts (ICA-AROMA) [39]. Finally, the non-steady first 10 s volumes were removed, and a bandpass filter was applied with a range of 0.008–0.1 Hz.

ii) PET data

The PET images were preprocessed as follows. Raw PET images were coregistered across different frames to reduce the motion effect, and then the frames over 5-min intervals were averaged. These images were reoriented to conform to a standard image grid of $160 \times 160 \times 96$ matrix with 1.5 mm^3 voxel size, and intensity normalization was performed. Spatial smoothing was applied with 8 mm FWHM. Further details are given on the ADNI website (<https://adni.loni.usc.edu/data-samples/adni-data/neuroimaging/pet/>). The PET images were coregistered to the corresponding T1w image with six degrees of freedom and subsequently nonlinearly registered onto the standard MNI space.

Imputation of time to conversion

The time taken to convert to AD can be considered the survival time commonly found in medical studies [34, 35, 40]. In clinical trials and longitudinal studies, a subject may experience a particular event, such as death or disease onset. The longitudinal data collected by the ADNI are suitable for survival analysis, as the study was conducted on the same subjects, and the time to conversion to AD can be utilized as a response variable. Identifying individuals at heightened risk of conversion to AD presents several research challenges, particularly the issue

of precisely determining the timing of conversion to AD. Since the time to conversion to AD is interval-censored, we are certain that conversion occurred within the interval between the date of the last MCI diagnosis and that of the first AD diagnosis. The time to conversion to AD was estimated based on the imputed survival times. A Weibull accelerated failure time (AFT) model with clinical covariates was fitted using the *icenReg* R package [41]. After imputation, interval-censored data were converted into right-censored data so that conventional survival analyses could be applied.

Functional connectivity gradient estimation

We estimated cortex-wide FC gradients and subcortical-weighted manifold degrees from baseline fMRI data. We used the Schaefer atlas with 200 parcels for the cortex [42] and the Desikan-Killiany atlas for the subcortex [43]. First, FC matrices were generated by calculating Pearson's correlations of the time-series signals between two distinct brain regions for each individual. Fisher's *r*-to-*z* transformation was applied to the individual-level matrices. A group-level connectivity matrix for the ADNI samples was constructed by averaging the individual connectivity matrices. This group connectivity matrix was subsequently thresholded, retaining only the top 10% of elements per row. An affinity matrix was then computed using a normalized angle kernel, which helped capture the similarity in connectivity patterns between cortical regions. We estimated low-dimensional eigenvectors (i.e., gradients) from the affinity matrix using diffusion map embedding [44], which is a nonlinear manifold learning technique. The diffusion map embedding algorithm is robust to noise and provides better computational efficiency than other nonlinear manifold learning techniques [45, 46]. We followed the diffusion map parameter settings used in previous studies [30, 47]. After constructing the ADNI group-level gradients, we aligned them to the group-level gradients of an independent Human Connectome Project (HCP) database (https://github.com/CAMIN-neuro/caminopen/tree/master/gradient_align) [48], which was derived using the procedure for the ADNI dataset. This further alignment mitigated the bias of demographic attributes specific to the ADNI dataset and stabilized the manifold [49]. The computed group-level gradients were then used as templates for the individual-level gradient alignment. Alignment was accomplished using Procrustes rotation [50]. The entire gradient estimation process was performed using the BrainSpace toolbox (<https://github.com/MICA-MNI/BrainSpace>) [51]. For subcortical regions, we estimated subcortical-weighted manifolds through element-wise multiplication of subcortico-cortical functional connectivity and cortical gradients [29, 30]. The nodal degree

was then computed, which effectively reflected the sub-cortico-cortical functional connectivity weighted by the cortical eigenvectors. We used the first two dominant cortical gradients, G1 and G2, along with the two corresponding subcortical-weighted manifold degrees, S1 and S2.

PET-SUVR estimation

PET scans enable the visualization of amyloid plaques and the assessment of glucose metabolism and tau spreading in the brain, offering information about the underlying pathological changes in AD. The standardized uptake value ratio (SUVR) for PET images was calculated using the cerebellum or brainstem as the reference region. Voxel values corresponding to the regions of interest (ROIs) defined by the atlases, specifically the Schaefer atlas [42] for cortical regions and the Desikan-Killiany atlas [43] for subcortical areas, were averaged and subsequently divided by the reference value. Following previous studies [52, 53], the reference regions were defined as the whole cerebellum for AV45, FBB, and tau-PET, and the brainstem for FDG-PET. These values within each ROI yielded regional SUVR values. Additionally, to facilitate the comparability of AV45-PET and FBB-PET measurements, we transformed their SUVR into centiloid (CL) units using the established transformation formula (<https://adni.loni.usc.edu/wp-content/themes/freshnews-dev-v2/documents/pet/ADNI%20Centiloids%20Final.pdf>). Finally, we calculated the global PET tracer score by averaging the regional SUVR values across all ROIs.

Prediction of conversion to AD

We applied a penalized Cox regression model with an elastic net penalty to analyze the time to conversion to AD, using FC manifolds as regressors. In the survival analysis framework, we have data in the form (y_i, x_i, δ_i) , where y_i is the observed survival time and δ_i is the indicator variable for the censoring of the i^{th} sample. Further, we assume $t_1 < t_2 < \dots < t_m$ be the increasing unique survival times. The common Cox proportional hazards model [54] assumes a semiparametric form for the hazard:

$$h_i(t) = h_0(t) \exp(\beta^T x), \tag{1}$$

where $h_0(t)$ is the baseline hazard at time t , $x = (x_1, x_2, \dots, x_p)$ is the column vector of the regression predictors, and $\beta = (\beta_1, \beta_2, \dots, \beta_p)^T$ is the vector consisting of the regression coefficients. The estimation of β is achieved by maximizing the partial likelihood,

$$L(\beta) = \prod_{i=1}^m \frac{e^{\beta^T x_{j(i)}}}{\sum_{j \in R_i} e^{\beta^T x_j}}, \tag{2}$$

where R_i is the risk set at the time t_i , consisting of indices j such that $y_j \geq t_i$. The performance of the survival model was evaluated using the concordance index (C-index), which indicates how well the model predicts the ordering of times for a specific event. Because the estimated FC manifolds have high dimensionality, penalized models may be a more efficient approach. In penalized regression, the least absolute shrinkage and selection operator (LASSO) [55] method, characterized by an L1-penalty, along with the ridge [56] method using an L2-penalty, is typically employed. Ridge regression is particularly effective in addressing multicollinearity among features, whereas LASSO reduces dimensionality by reducing regression coefficients to zero. An elastic net [57] penalty combines the advantages of both LASSO and the ridge, providing an optimal solution. We estimated the β via the coordinate descent algorithm using the glmnet R package [58]. In our study, we denote $x = (x_{(1)}, x_{(2)})$ where $x_{(1)}$ is the FC manifold vector, and $x_{(2)}$ indicates the clinical variable vector. To control for the potential effects of the demographic and clinical variables $x_{(2)}$ including age, sex, MMSE, APOE4 status, and education level, we considered these as additional covariates and imposed the penalty term only on the FC manifold $x_{(1)}$. Accordingly, $\beta_{(1)} = (\beta_1, \dots, \beta_q)^T$ and $\beta_{(2)} = (\beta_{q+1}, \dots, \beta_p)^T$ are regression coefficients for the FC manifolds and the clinical variables, respectively. We defined a linear combination of $\beta^T x$ as the risk score. In summary, we used FC manifolds (G1, S1, G2, and S2) and controlled for covariates as regression predictors. In our model, β can be estimated by maximizing the partially imposed penalized log partial likelihood $l(\beta) = \log(L(\beta))$,

$$\hat{\beta} = \operatorname{argmax}_{\beta} [l(\beta) - \lambda P_{\alpha}(\beta_{(1)})] = (\hat{\beta}_{(1)}, \hat{\beta}_{(2)}), \tag{3}$$

where

$$P_{\alpha}(\beta_{(1)}) = (\alpha \sum |\beta_{(1)}| + \frac{1}{2} (1 - \alpha) \sum \beta_{(1)}^2), \quad (0 \leq \alpha \leq 1). \tag{4}$$

The input feature scale is normalized using the mean and standard deviation. For model estimation, we implemented a five-fold cross-validation to select hyperparameters: L1-ratio α and regularization parameter λ . Hyperparameter selection was based on the highest C-index derived from the cross-validation procedure. This procedure was repeated 20 times, and the resulting outcomes were reported. For robustness, we averaged the estimated coefficients and risk scores from all optimally

identified models. To assess the effect size related to the conversion to AD, we calculated the region-wise sum of the absolute coefficients of the FC manifolds (G1 and G2 or S1 and S2). This effect quantifies the extent to which an alteration in the functional connectivity of a region influences the likelihood of conversion to AD while controlling for other covariates.

Survival analyses of conversion to AD

We stratified participants at risk of conversion to AD into fast and slow conversion groups based on a zero cutoff of the predicted risk score and assessed between-group differences between the two groups using a log-rank test. To further examine whether PET scores were different between the two groups, we compared averaged global amyloid- β positivity (i.e., CL), glucose metabolism, and tau accumulation derived from PET scans between the groups using the Wilcoxon rank-sum test.

Considering the longitudinal nature of the data, the trajectory of the conversion to AD was traced for each participant. We identified four potential trajectories for participants at risk of conversion to AD: CN to MCI, MCI to censored MCI, CN (or via MCI) to AD, and MCI to AD. We denoted the progression paths from the diagnosis at the time of the baseline scan to either AD conversion or the last follow-up with an arrow (e.g., MCI \rightarrow AD). We used a t-test to compare differences between the groups based on diagnosis at the time of the scan and an analysis of variance (ANOVA) with a post hoc analysis based on the Tukey honest significant difference test to compare differences between the conversion trajectories. Finally, the associations between the risk scores and both the clinical dementia rating sum of boxes (CDRSB) and Alzheimer's Disease Assessment Scale (ADAS) were explored. The CDRSB is a widely used tool that quantifies the severity of dementia symptoms across multiple domains, while the ADAS provides a comprehensive assessment of the cognitive and non-cognitive functions of AD.

Robustness analyses and external validation

To demonstrate the robustness of our findings, we conducted sensitivity analyses using several methodologies. First, we considered the ridge penalty along with the elastic net penalty as an alternative to the penalized Cox regression model. Second, we separately fit the models using only the first (G1 and S1) and second (G2 and S2) manifolds. Third, while estimating the functional gradients, we applied different thresholds by retaining 5% and 15% of the elements per row in the FC matrix.

We validated our findings using an external validation dataset obtained from the OASIS3 database [33]. The replication involved two external validation sets: (1)

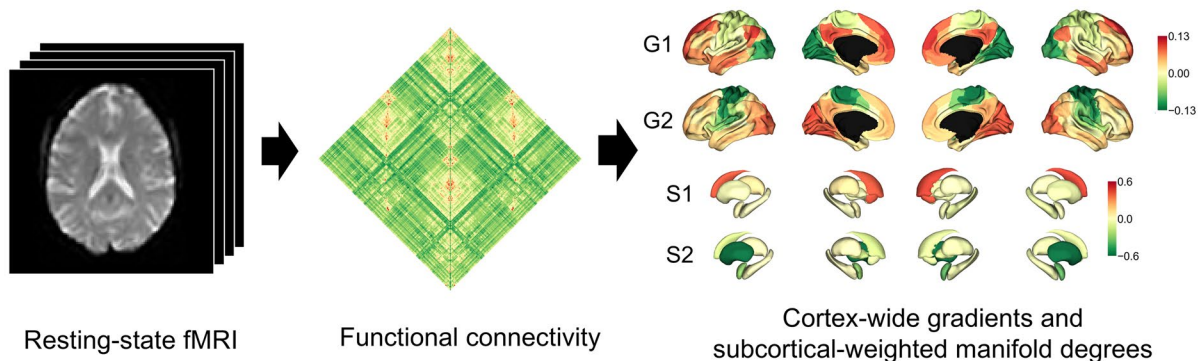
the *OASIS risk dataset* (longitudinal) and (2) the *OASIS diagnosis dataset* (cross-sectional). (1) The *OASIS risk dataset* was created using the same participant selection criteria as that used in the *ADNI risk dataset* and was designed for external validation purposes. (2) The *OASIS diagnosis dataset* contained labels (CN, MCI, and AD) based on the corresponding diagnoses. We estimated the FC gradients from both datasets using the same procedure as that used for the *ADNI risk dataset* and aligned the individual gradients to the ADNI-to-HCP gradient template. Subsequently, the aligned FC gradients and subcortical-weighted manifold degrees were estimated. We then normalized the FC manifolds and demographic and clinical covariates using the mean and standard deviations derived from the *ADNI risk dataset*. We predicted the risk scores for the two external validation datasets from all identified models from 20 iterations and averaged the risk scores. For the *OASIS risk dataset*, we fit another Weibull AFT model using clinical covariates from the *OASIS risk dataset* and estimated the time to conversion to AD. We evaluated the C-index and stratified the participants into fast and slow conversion groups using a zero threshold. We then examined their conversion trajectories and risk scores. For the *OASIS diagnosis dataset*, we evaluated the risk score distribution for the CN, MCI, and AD groups and tested for significant differences among them. We also analyzed the association between the risk scores and CDRSB.

Results

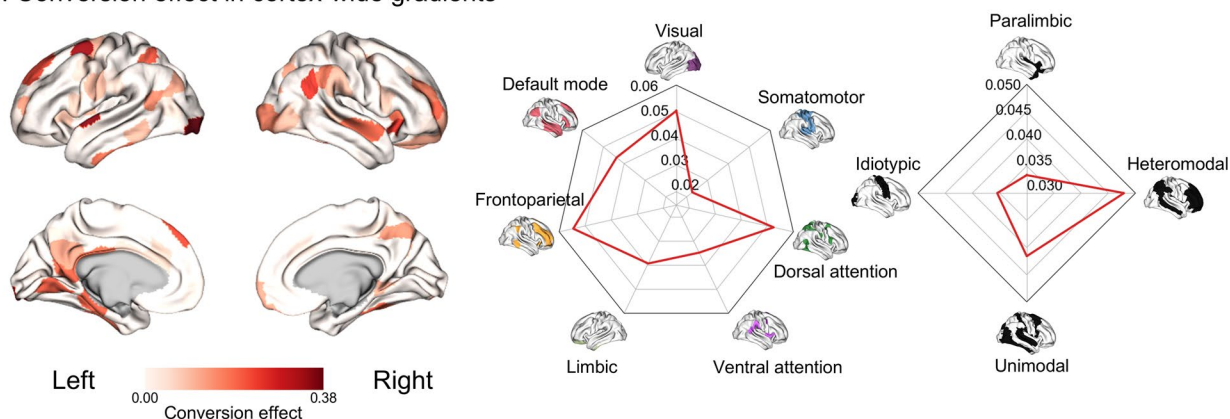
Whole-brain functional connectivity gradients

To reveal the functional connectome organization of the brain, we applied dimensionality reduction techniques to the FC matrix and generated multiple low-dimensional eigenvectors, referred to as gradients [27, 59, 60]. The FC gradients exhibited smooth transitions along the cortical surface, where the first principal gradient (G1) presented a gradual axis with sensory and motor systems at one end and transmodal regions, such as the default mode and frontoparietal networks, at the other end (Fig. 1A). The second gradient (G2) differentiated the somatomotor regions from the visual system. The first two functional gradients (G1, G2) accounted for approximately 37.2% of the information in the input connectivity matrix, and a large eigengap was identified between the second and third components, indicating the first two gradients are dominant (Supplementary Fig. 1). In addition to the cortico-cortical connectivity gradients, we generated two subcortical-weighted manifold degrees (S1 and S2) by projecting the strength of subcortical regions onto the cortical manifold space to assess connectivity changes in the subcortical regions (Fig. 1A) [29, 30].

A. Whole-brain functional connectivity manifolds



B. Conversion effect in cortex-wide gradients



C. Conversion effect in subcortical-weighted manifold degrees

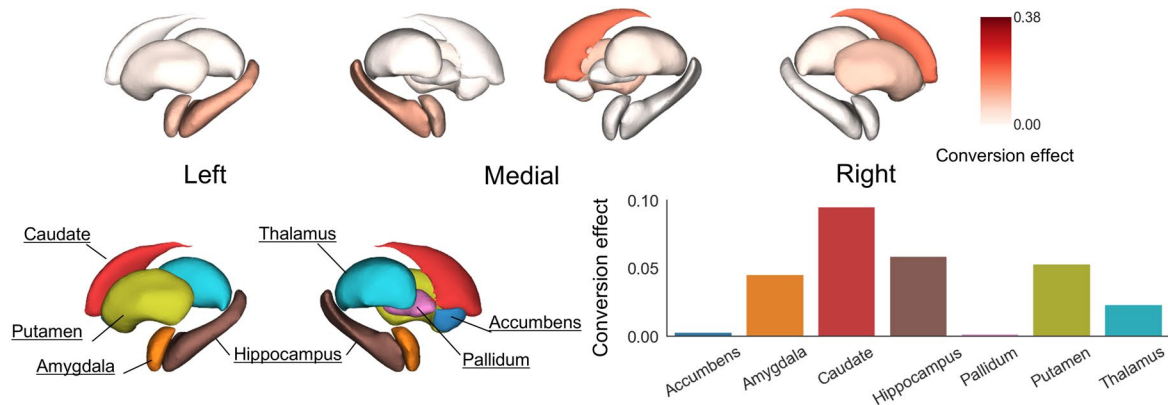


Fig. 1 Functional connectivity manifolds and the conversion effects of AD. **A** Functional connectivity gradients (G1 and G2) and subcortical-weighted manifold degrees (S1 and S2) were estimated from the functional connectivity matrix computed from the resting-state functional MRI (rs-fMRI). **B** The conversion (CN/MCI to AD) effects estimated by penalized Cox regression are mapped on the cortical surface. We stratified the effects according to seven intrinsic functional communities and four cortical hierarchical levels. **C** The conversion effects of subcortical-weighted manifold degrees are displayed on each subcortical structure. *Abbreviations:* MRI, magnetic resonance imaging; CN, cognitive normal; MCI, mild cognitive impairment; AD, Alzheimer's disease

Prediction of conversion risk for AD

We leveraged penalized Cox regression with FC manifolds (i.e., cortical gradients and subcortical-weighted

manifold degrees) to predict the overall prognosis of individuals at risk of conversion to AD. Progressive neurodegeneration was quantified using the regression coefficient

estimated by maximizing the partial likelihood function. We found altered FC manifolds in individuals at risk of conversion to AD. Pronounced conversion effects (i.e., regression coefficients) were observed in multiple cortical regions, including the visual, frontoparietal, and temporal regions (Fig. 1B), as well as in the subcortical areas of caudate and hippocampus (Fig. 1C). To recapitulate which brain regions showed higher conversion effects according to functional brain networks or cortical hierarchical levels, we summarized the conversion effects according to seven functional communities, which show a comprehensive overview of the organizational principle of functional connectivity [61], and four hierarchical levels, indicating cortical hierarchy expanding from low-level sensory to higher-order cognitive control brain regions [62]. Our findings suggest that functional vulnerability notably impacts sensory/motor relay, cognitive control processing, memory, and emotional regulations.

Survival analysis based on the predicted conversion risk

To identify the effects of conversion to AD, we defined the risk score by calculating a linear combination of the regression coefficient, predictors of FC manifolds, and clinical variables. Based on the risk score, we determined the fast and slow conversion groups and compared survival probabilities between the groups. Notably, the two subgroups exhibited distinct conversion pathways for AD (log-rank test, $p < 0.0001$; Fig. 2A). The median conversion date for the fast conversion group was 633 days (549–754 days; 95% confidence interval), whereas it exceeded five years for the slow conversion group. When we compared the FC manifolds between the slow and fast conversion groups, significant between-group differences were observed in the visual cortex and the putamen (Supplementary Fig. 2), suggesting that the slow and fast conversion groups exhibit distinct functional organizational profiles in the sensory regions.

PET tracer score comparison between the slow and fast conversion groups

We also compared the distributions of amyloid- β positivity, glucose metabolism, and tau accumulation derived from the PET tracer scans between the fast and slow conversion groups. We compared the averaged amyloid- β PET CL, FDG-PET SUVR, and tau-PET SUVR between the groups. We found significant differences in the amyloid- β PET CL ($p = 0.006$), FDG-PET SUVR ($p = 0.005$), and tau-PET SUVR ($p = 0.014$; Fig. 2B). The findings indicate that the groups defined using the predicted conversion risk show metabolically and pathologically different effects by PET.

Risk score-based stratification of disease conversion trajectories

Although the risk score showed no significant difference based on the diagnosis at the time of the scan ($p = 0.066$), a distinct difference in the risk score was observed when the disease trajectory was segmented according to the longitudinal attributes of our dataset ($p < 0.001$; Fig. 2C). The group progressing from MCI to AD (MCI \rightarrow AD) demonstrated a higher risk score than the group with MCI with no progression to AD (MCI \rightarrow MCI). Furthermore, the MCI-to-AD group, with a more imminent conversion to AD than the CN-to-AD group (CN \rightarrow AD), exhibited a higher risk score, even though both groups ultimately progressed to AD.

Clinical implications of the risk score

We associated the risk score with several clinical scores to assess whether it could be used as a surrogate marker. The predicted risk score was strongly correlated with the CDRSB ($r = 0.535$, $p < 0.001$), ADAS 11 ($r = 0.425$, $p < 0.001$), and ADAS 13 ($r = 0.464$, $p < 0.001$) scores (Fig. 2D). The results confirmed that the more severe the dementia symptoms, the higher the risk score.

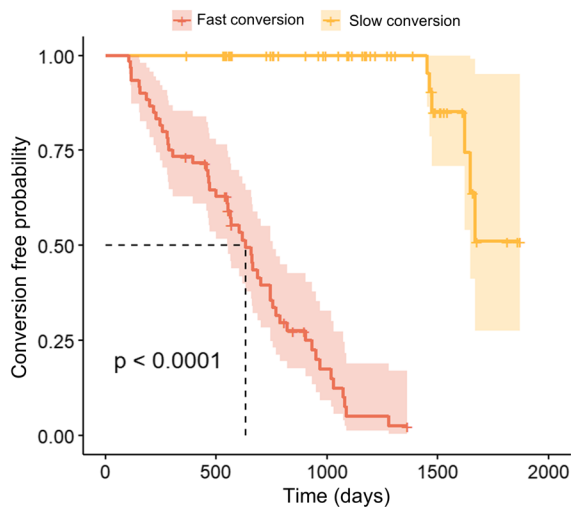
Group-level comparison of AD converters vs. non-converters

Multivariate testing was conducted using a two-element manifold vector (i.e., G1+S1, G2+S2) between AD converters and non-converters after controlling for age, sex, MMSE score, APOE4 status, and education length to better understand our approach to integrating time information. We found that the visual cortex and striatum showed significant between-group differences (Supplementary Fig. 3). These regions were slightly different from the conversion effects, which may be explained by the fact that this group stratification approach did not effectively incorporate time-related information. In addition, such group comparisons require caution when setting the group-level contrast, because if the time window for AD non-converters is extended, they could become converters.

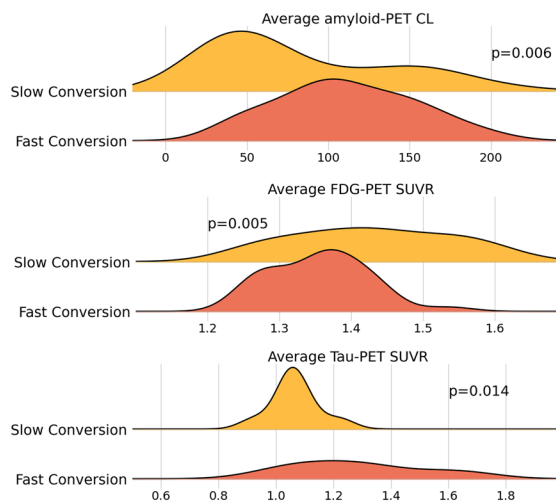
Evaluation of model robustness

To demonstrate the robustness of our findings regarding FC manifolds with respect to our methodological choices, we performed several sensitivity analyses. We performed a penalized Cox regression using the ridge penalty instead of the elastic net penalty. When employing the ridge penalty, the conversion effect was pronounced in the visual and frontoparietal, attention networks as well as in the putamen and caudate (Supplementary Fig. 4). Additionally, we separately fitted

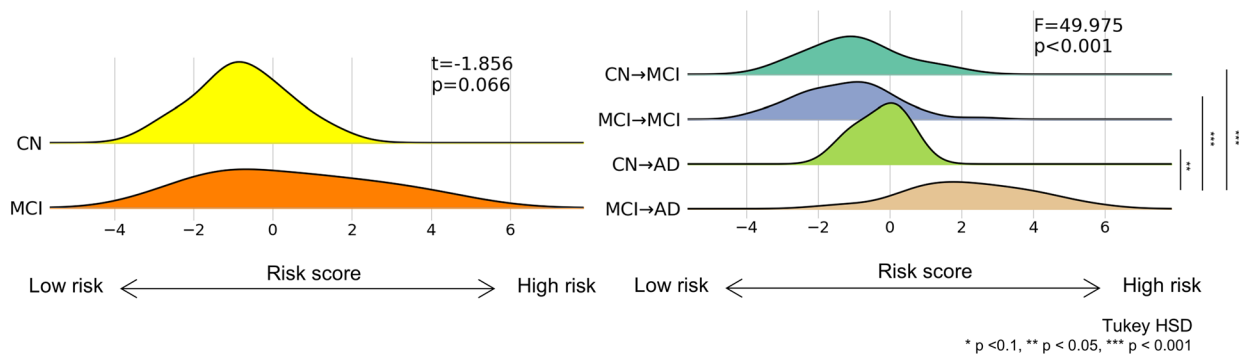
A. Survival analysis between slow and fast conversion groups



B. PET tracer distribution



C. Differences in risk score based on diagnosis and conversion trajectory



D. Associations between the risk score and clinical phenotypes

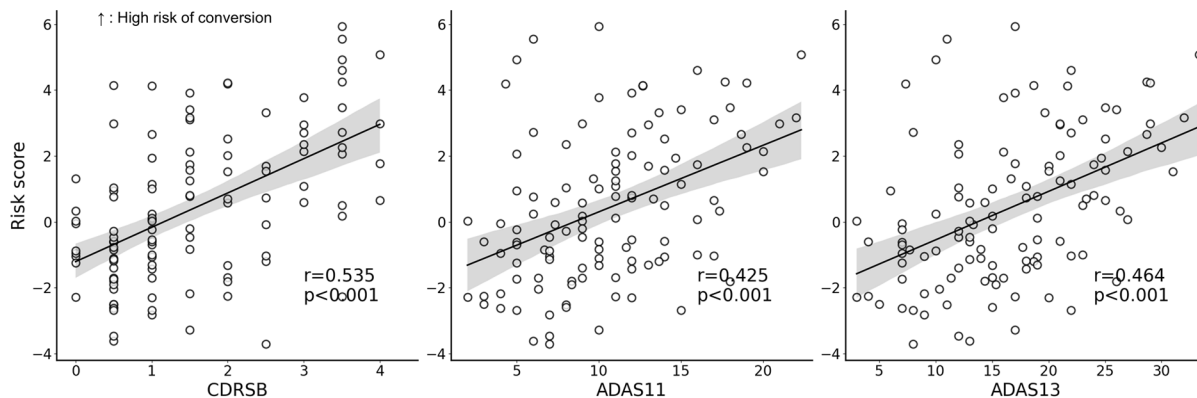


Fig. 2 Analysis of conversion risk scores. **A** Kaplan–Meier plot stratifying fast and slow conversion groups. **B** Comparison of PET tracer distributions between the two groups. **C** Differences in risk scores based on diagnosis at the time of scanning (left) and those according to the trajectory of the conversion to AD (right). **D** Associations between risk scores and clinical scores. *Abbreviations:* PET, positron emission tomography; CL, centiloid; SUVR, standardized uptake value ratio; FDG-PET, ¹⁸F-fluorodeoxyglucose-PET; tau-PET, ¹⁸F-Flortaucipir-PET; CN, cognitive normal; MCI, mild cognitive impairment; AD, Alzheimer’s disease; Tukey HSD, Tukey honestly significant difference; CDRSB, clinical dementia rating sum of boxes; ADAS, Alzheimer’s disease assessment scale

the penalized Cox regression models using G1+S1 and G2+S2. The C-index was smaller when only the first or second FC manifold was considered compared with the combined FC manifolds (Supplementary Table 4). Our results underscore the value of employing combined manifolds for enhanced performance and a holistic understanding of the whole brain. Finally, when we changed the threshold values of FC to 5% and 15%, the spatial patterns of the gradients and the conversion effect were largely consistent, with spatial correlations between the main (i.e., 10% threshold) conversion effect and those of 5% and 15% thresholds being $r=0.61$ and 0.74 ($p < 0.05$; Supplementary Figs. 5 and 6).

Validation using external datasets

Our findings from the *ADNI risk dataset* were successfully validated using external datasets, confirming that our FC manifolds can serve as prognostic biomarkers for AD. The median conversion date of the *OASIS risk dataset* was 271 days, with a conversion rate of 66.6%. In the *OASIS risk dataset*, the prognostic accuracy achieved a C-index of 0.716 ± 0.015 , and survival curves between the fast and slow conversion groups were significantly different (log-rank test, $p=0.019$; Fig. 3A left). The median conversion dates for the fast and slow conversion groups were 89 and 1,166 days, respectively. Furthermore, the stratified trajectories demonstrated that the conversion from MCI to AD posed the highest risk, whereas the conversion from CN to MCI posed the lowest risk (Fig. 3A right). These two trajectories (MCI→AD and CN→MCI) showed marginal differences ($p=0.052$). In the *OASIS diagnosis dataset*, we observed significant between-group differences in risk scores among the CN, MCI, and AD groups ($p < 0.001$; Fig. 3B left). Notably, in the AD group, the risk score increased as the severity of dementia symptoms increased ($r=0.564$, $p < 0.001$; Fig. 3B right).

Discussion

The identification of reliable biomarkers for the conversion to AD from MCI or CN states is pivotal for timely therapeutic interventions. This study treated AD conversion as a survival problem, incorporating time to conversion and censorship. We found altered FC patterns across the cortical and subcortical regions in individuals vulnerable to AD conversion. The proposed risk score may serve as a biomarker for AD conversion because it correlates well with known disease trajectories, cerebral glucose metabolism, amyloid or tau pathology, and various clinical phenotype scores for symptom severity. The

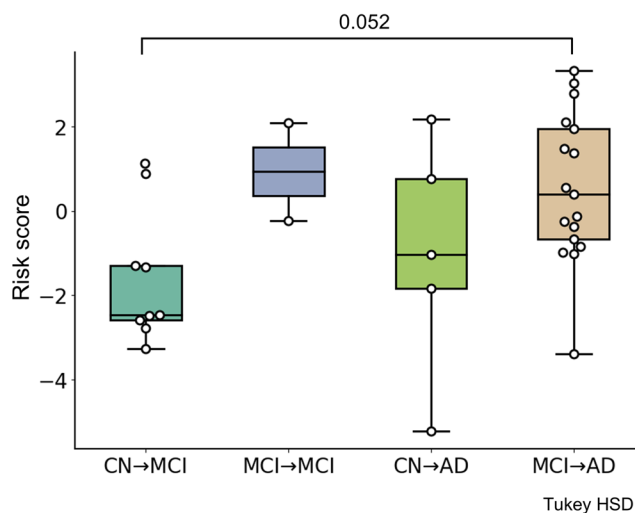
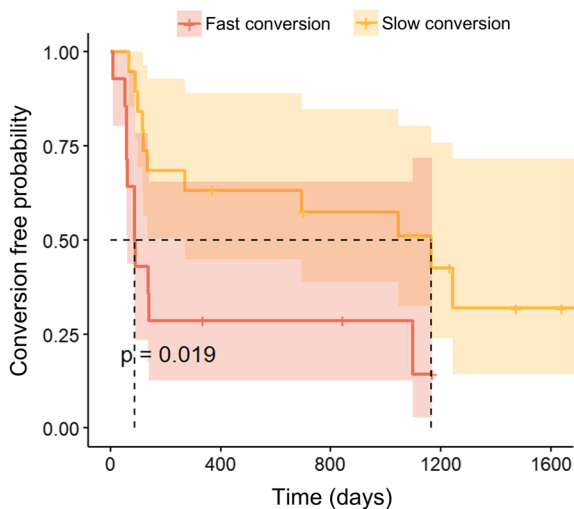
results were validated using an independent dataset, indicating the robustness of the proposed prognostic model.

We used connectome-manifold techniques to explore the progression of AD. This approach offers a robust and biologically interpretable perspective of the cortical axes, emphasizing the core components and facilitating analysis with essential information [27]. An FC gradient is a basis vector derived from a dimensionality reduction algorithm that can explain the original FC matrix well. A coefficient of arbitrary sign (positive or negative) is multiplied with the basis vector to actually represent the original FC. Thus, the sign of the gradients does not hold a specific meaning. Instead, the FC gradients should be understood as representing a continuous axis or dimension along which the FC varies. The purpose is to show the spatial organization of FC patterns rather than to indicate correlations or anti-correlations of functional time series. In addition, subcortico-cortical connectivity was assessed by projecting connectivity weights to cortical gradients [29, 30]. Using these FC manifolds, we identified the brain regions vulnerable to AD conversion. Notably, the sensory and frontoparietal cortices, caudate, and hippocampus were significantly affected. These areas are crucial for memory formation and navigation, and their decline is potentially due to amyloid deposition or neurofibrillary tangle formation [63–65]. It has been shown that dysfunction in the frontal-subcortical circuit, including the striatum, basal ganglia, and thalamus, is associated with neuropsychiatric disorders [66]. Indeed, dysconnectivity between the hippocampus and prefrontal cortex has been linked to cognitive decline in AD [67]. In addition, subcortical regions of the hippocampus and caudate affect memory systems, and their degradation may be linked to memory loss [68–72].

Interestingly, the conversion effects showed asymmetric patterns between the left and right hemispheres. FC manifolds often exhibit similar values across the hemispheres, yet in some cases, one side may have more influence. We applied penalized regression to FC manifolds where only one region would be selected if two regions across hemispheres exhibit similar trends. This is because of the high correlation of the features between the two hemispheres, leading to highly asymmetric conversion patterns. We believe the asymmetry of the conversion effects might partly come from our methodological choice of penalized regression. However, systematic analyses exploring the inter-hemispheric asymmetry of FC in AD can be performed in future studies to unveil topological underpinnings of AD connectopathology.

The potential clinical utility of the generated risk scores was validated in several respects. First, we defined fast

A. OASIS Risk Dataset



B. OASIS Diagnosis Dataset

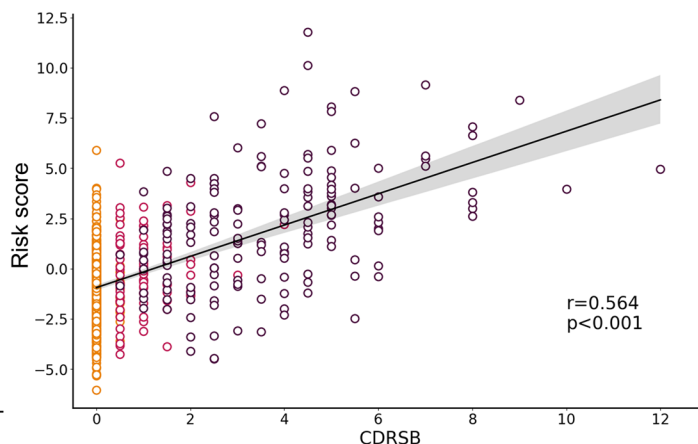
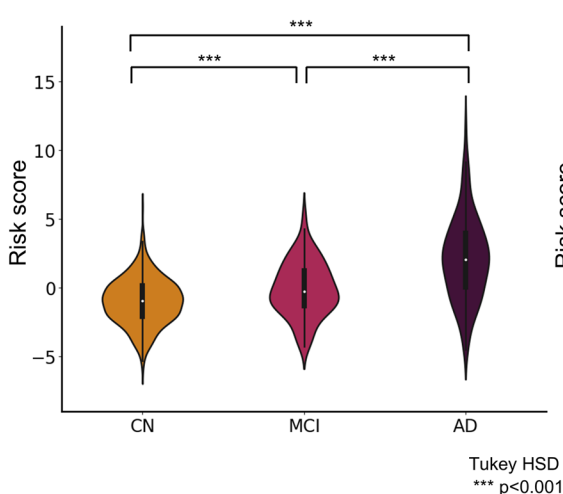


Fig. 3 External validation results. **A** Kaplan–Meier plot stratifying fast and slow conversion groups (left) and the differences in risk scores according to the trajectory of the conversion to AD (right) in the OASIS risk dataset. **B** Risk score distributions based on the diagnosis (left) and the association between risk score and clinical dementia rating scales (right) in the OASIS diagnosis dataset. The color of the dots in the scatter plot is the same as the diagnosis group. Abbreviations: CN, cognitive normal; MCI, mild cognitive impairment; AD, Alzheimer’s disease; Tukey HSD, Tukey honest significant difference; CDRSB, clinical dementia rating sum of boxes

and slow conversion groups based on the risk score. The groups followed distinct pathways to AD, each characterized by different amyloid- β deposition, cerebral glucose metabolism, and tau accumulation patterns. Notably, fast converters exhibited more extensive tau pathology and higher amyloid- β plaque burden compared to slow converters. Indeed, a study highlights that cognitively unimpaired individuals with both amyloid- β plaques and tau tangles detected by PET imaging face significantly higher risks of cognitive decline and progression to mild cognitive impairment [73–75]. In addition, previous

studies have shown that AD is associated with significant glucose hypometabolism in the posterior cingulate cortex, which is predominantly affected by the disease [76–79]. The fast conversion group exhibited a greater reduction in cerebral glucose metabolism than the slow conversion group, indicating that the onset of hypometabolism derived from FDG-PET can be used to predict AD conversion [80, 81]. Moreover, we observed variations in functional organization between the fast and slow conversion groups, suggesting that distinct macroscale connectome architectures may correspond with

their respective conversion rates to AD. These differences highlight the foundational role of functional connectivity in influencing the varying rates of conversions. However, more elaborate analyses are required to systematically evaluate between-group differences in FC between the fast and slow conversion groups.

Next, we segmented the conversion trajectories and found that individuals more vulnerable to AD conversion had higher risk scores. These findings suggest that FC manifolds and risk scores could be used as quantitative prognosis prediction markers in clinical practice, allowing early diagnosis and the implementation of timely treatment plans. However, it should be noted that the *ADNI risk dataset's* risk score of the MCI → MCI group and the CN → AD group did not show significant differences ($p=0.610$; Fig. 2C right). Similarly, the *OASIS risk dataset* did not exhibit significant differences between the groups ($p=0.394$; Fig. 3A right). Risk scores were not statistically different between individuals who remained stable in the MCI stage (MCI → MCI) and those who converted from CN to AD (CN → AD). The comparable risk scores may indicate that participants in the MCI stage are heterogeneous, with some individuals at high risk of rapid progression (similar to CN → AD converters) and others with more resilience or compensatory mechanisms that keep them stable for longer periods. This observation suggests that there could be other factors influencing the progression from MCI to AD, including genetic predispositions. It highlights the need for a more detailed exploration of the diverse factors that determine the progression trajectories in AD. Moreover, clinical scores, such as the CDRSB and ADAS, which measure cognitive function [82], were significantly correlated with the risk score, again indicating a clinically reliable marker. Multiple sensitivity analyses and external data validation confirm the credibility of the proposed model.

In the current analysis, there are potential limitations. First, it has been shown that changes in vascular dysregulation (measured with arterial spin labeling [ASL] imaging) and amyloid- β deposition (measured with PET) might occur before fMRI-related changes [10]. However, limited samples with ASL imaging met our inclusion criteria in the ADNI database hindered the analysis of vascular dysregulation. More delicate analyses should be performed in future works by integrating multiple imaging modalities to assess molecular and macroscale brain disorganization in AD. Second, our study may have included individuals assessed as CN or diagnosed with MCI before inclusion, leading to a left truncation. However, our analysis treated these individuals as if they had entered the study at the time of diagnosis, which may have led to an underestimation or overestimation of their time at risk. While our model is capable of handling

right censoring, it does not explicitly account for left truncation. This limitation may have introduced biased estimates of the regression coefficients and survival probabilities. Third, with limited samples, some samples taken after the initial scan of the same individual were assumed to be independent. However, these samples are likely to be correlated. In future studies, incorporating left-truncated data and accounting for correlations between repeated measurements in a large study population will enhance the accuracy of survival estimates and provide a more comprehensive understanding of the risk factors associated with conversion to AD.

Conclusions

In the present study, we developed a prognostic model for predicting the risk of conversion from MCI (or CN) to AD by leveraging functional connectivity and Cox regression. With a high C-index, our model underscores the significance of whole-brain manifolds in AD conversion. Furthermore, the risk score, which correlates with cerebral glucose metabolism, amyloid or tau pathology, and clinical phenotype scores, may be a promising tool for clinicians. Our risk score distinguished between the fast and slow conversion groups, and the association of this risk score with established cognitive function measures emphasized its potential clinical utility. Identifying reliable and high-performance biomarkers for predicting AD conversion allows earlier detection of at-risk individuals with MCI or subjective memory concerns, enabling timely therapeutic interventions.

Abbreviations

AD	Alzheimer's disease
ADAS	Alzheimer's disease assessment scale
ADNI	Alzheimer's disease neuroimaging initiative
AFT	Accelerated failure time
APOE4	Apolipoprotein E4
ASL	Arterial spin labeling
AV45-PET	^{18}F -florbetapir-PET
CDRSB	Clinical dementia rating sum of boxes
CL	Centiloid
CN	Cognitively normal
EPI	Echo planar imaging
FBB-PET	^{18}F -florbetaben-PET
HCP	Human connectome project
FC	Functional connectivity
FDG-PET	^{18}F -fluorodeoxyglucose-PET
FWHM	Full-width half-maximum
ICA-AROMA	Independent component analysis-based automatic removal of motion artifacts
IRB	Institutional review board
MCI	Mild cognitive impairment
MMSE	Mini-mental state examination
MPRAGE	Magnetization-prepared rapid acquisition gradient echo
OASIS	Open access series of imaging studies
PET	Positron emission tomography
SUVr	Standardized uptake value ratio
T1w	T1-weighted
TE	Echo time
TR	Repetition time
rs-fMRI	Resting-state functional magnetic resonance imaging

Supplementary Information

The online version contains supplementary material available at <https://doi.org/10.1186/s13195-024-01589-3>.

Supplementary Material 1.

Acknowledgements

Funding: Dr. Bo-yong Park was supported by the Institute for Information and Communications Technology Planning and Evaluation (IITP), funded by the Korean Government (MSIT) (No. 2022-0-00448/RS-2022-II220448, Deep Total Recall: Continual Learning for Human-Like Recall of Artificial Neural Networks). Dr. Hyunjin Park was supported by National Research Foundation (NRF-2020M3E5D2A01084892), AI Graduate School Support Program (Sungkyunkwan University) (RS-2019-II190421), ICT Creative Consilience program (RS-2020-II201821). Dr. Hyunjin Park and Dr. Bo-yong Park were jointly supported by the IITP funded by the Korean Government (MSIT) (RS-2021-II212068, Artificial Intelligence Innovation Hub) and the Institute for Basic Science (IBS-R015-D1). Acknowledgements: Data collection and sharing for this project were funded by the Alzheimer's Disease Neuroimaging Initiative (ADNI) (National Institutes of Health Grant U01 AG024904) and the DOD ADNI (Department of Defense award number W81XWH-12-2-0012). ADNI is funded by the National Institute on Aging, the National Institute of Biomedical Imaging and Bioengineering, and through generous contributions from the following: AbbVie, Alzheimer's Association; Alzheimer's Drug Discovery Foundation; Araclon Biotech; BioClinica, Inc.; Biogen; Bristol-Myers Squibb Company; CereSpir, Inc.; Cogstate; Eisai Inc.; Elan Pharmaceuticals, Inc.; Eli Lilly and Company; EuroImmun; F. Hoffmann-La Roche Ltd and its affiliated company Genentech, Inc.; Fujirebio; GE Healthcare; IXICO Ltd.; Janssen Alzheimer Immunotherapy Research & Development, LLC.; Johnson & Johnson Pharmaceutical Research & Development LLC.; Lumosity; Lundbeck; Merck & Co., Inc.; Meso Scale Diagnostics, LLC.; NeuroRx Research; Neurotrack Technologies; Novartis Pharmaceuticals Corporation; Pfizer Inc.; Piramal Imaging; Servier; Takeda Pharmaceutical Company; and Transition Therapeutics. The Canadian Institute of Health Research provided funds to support the ADNI clinical sites in Canada. Private-sector contributions were provided by the Foundation for the National Institutes of Health (www.fnih.org). The grantee organization was the Northern California Institute for Research and Education, and the study was coordinated by the Alzheimer's Therapeutic Research Institute at the University of Southern California. ADNI data were disseminated by the Laboratory for Unk Imaging at the University of Southern California. Data were provided by OASIS3: Principal Investigators: T. Benzinger, D. Marcus, J. Morris; NIH P30 AG066444, P50 AG00561, P30 NS09857781, P01 AG026276, P01 AG003991, R01 AG043434, UL1 TR000448, R01 EB009352. AV-45 doses were provided by Avid Radiopharmaceuticals, a wholly-owned subsidiary of Eli Lilly.

Authors' contributions

S.K., B.P., and H.P. designed the study, analyzed the data, and wrote the manuscript. M.K. and J.L. assisted with the experiments and reviewed the manuscript. B.P. and H.P. are the corresponding authors for this study and are responsible for the integrity of the data analysis. All authors reviewed and approved the final version of the manuscript for publication.

Availability of data and materials

Imaging and phenotypic data were provided in part by the Alzheimer's Disease Neuroimaging Initiative (<https://adni.loni.usc.edu>) and the Open Access Series of Imaging Studies (<https://www.oasis-brains.org/>)

Declarations

Ethics approval and consent to participate

Institutional Review Board (IRB) approvals were obtained from the original study depicting the ADNI and OASIS databases. In the ADNI dataset, consent forms were approved by each participating site's IRB. The IRB of Washington University School of Medicine approved the OASIS study and written informed consent were obtained for all participants. All ADNI and OASIS datasets have been fully anonymized, with no protected health information included. All procedures performed in studies involving human participants were in accordance with the ethical standards of the institutional and/or national

research committee and with the 1964 Helsinki Declaration and its later amendments or comparable ethical standards.

Consent for publication

All authors agreed for publication.

Competing interests

The authors declare no competing interests.

Author details

¹Department of Electrical and Computer Engineering, Sungkyunkwan University, Suwon, Republic of Korea. ²Center for Neuroscience Imaging Research, Institute for Basic Science, Suwon, Republic of Korea. ³Department of Artificial Intelligence, Gwangju Institute of Science and Technology, Gwangju, Republic of Korea. ⁴Department of Brain and Cognitive Engineering, Korea University, Seoul, Republic of Korea. ⁵School of Electronic and Electrical Engineering, Sungkyunkwan University, Suwon, Republic of Korea.

Received: 27 January 2024 Accepted: 29 September 2024

Published online: 09 October 2024

References

- Buchman AS, Bennett DA. Loss of motor function in preclinical Alzheimer's disease. *Expert Rev Neurother*. 2011;11(5):665–76.
- Holland D, et al. Subregional neuroanatomical change as a biomarker for Alzheimer's disease. *Proc Natl Acad Sci*. 2009;106(49):20954–9.
- Blennow K, de Leon MJ, Zetterberg H. Alzheimer's disease. *The Lancet*. 2006;368(9533):387–403.
- Graham JE, et al. Prevalence and severity of cognitive impairment with and without dementia in an elderly population. *The Lancet*. 1997;349(9068):1793–6.
- Eskildsen SF, et al. Structural imaging biomarkers of Alzheimer's disease: predicting disease progression. *Neurobiol Aging*. 2015;36:S23–31.
- Guerrero R, et al. Manifold population modeling as a neuro-imaging biomarker: application to ADNI and ADNI-GO. *Neuroimage*. 2014;94:275–86.
- Li H, et al. A deep learning model for early prediction of Alzheimer's disease dementia based on hippocampal magnetic resonance imaging data. *Alzheimers Dement*. 2019;15(8):1059–70.
- Nordberg A, et al. The use of PET in Alzheimer disease. *Nat Rev Neurol*. 2010;6(2):78–87.
- Rombouts SA, et al. Altered resting state networks in mild cognitive impairment and mild Alzheimer's disease: an fMRI study. *Hum Brain Mapp*. 2005;26(4):231–9.
- Iturria-Medina Y, et al. Early role of vascular dysregulation on late-onset Alzheimer's disease based on multifactorial data-driven analysis. *Nat Commun*. 2016;7(1):11934.
- Nestor PJ, Scheltens P, Hodges JR. Advances in the early detection of Alzheimer's disease. *Nat Med*. 2004;10(Suppl 7):S34–41.
- Ries ML, et al. Magnetic resonance imaging characterization of brain structure and function in mild cognitive impairment: a review. *J Am Geriatr Soc*. 2008;56(5):920–34.
- Putcha D, et al. Hippocampal hyperactivation associated with cortical thinning in Alzheimer's disease signature regions in non-demented elderly adults. *J Neurosci*. 2011;31(48):17680–8.
- Reiman EM, et al. Declining brain activity in cognitively normal apolipoprotein E $\epsilon 4$ heterozygotes: a foundation for using positron emission tomography to efficiently test treatments to prevent Alzheimer's disease. *Proc Natl Acad Sci*. 2001;98(6):3334–9.
- Landin-Romero R, et al. Disease-specific patterns of cortical and subcortical degeneration in a longitudinal study of Alzheimer's disease and behavioural-variant frontotemporal dementia. *Neuroimage*. 2017;151:72–80.
- Roh JH, et al. Volume reduction in subcortical regions according to severity of Alzheimer's disease. *J Neurol*. 2011;258:1013–20.
- de Jong LW, et al. Strongly reduced volumes of putamen and thalamus in Alzheimer's disease: an MRI study. *Brain*. 2008;131(12):3277–85.
- Wang K, et al. Altered functional connectivity in early Alzheimer's disease: A resting-state fMRI study. *Hum Brain Mapp*. 2007;28(10):967–78.

19. Dennis EL, Thompson PM. Functional brain connectivity using fMRI in aging and Alzheimer's disease. *Neuropsychol Rev.* 2014;24:49–62.
20. Damoiseaux JS, et al. Functional connectivity tracks clinical deterioration in Alzheimer's disease. *Neurobiol Aging.* 2012;33(4):828–e19–828. e30.
21. Sorg C, et al. Selective changes of resting-state networks in individuals at risk for Alzheimer's disease. *Proc Natl Acad Sci.* 2007;104(47):18760–5.
22. Wang L, et al. Changes in hippocampal connectivity in the early stages of Alzheimer's disease: evidence from resting state fMRI. *Neuroimage.* 2006;31(2):496–504.
23. Hu Q, et al. Brain network hierarchy reorganization in Alzheimer's disease: A resting-state functional magnetic resonance imaging study. *Hum Brain Mapp.* 2022;43(11):3498–507.
24. Shen, L, et al. Identifying neuroimaging and proteomic biomarkers for MCI and AD via the elastic net. in *Multimodal Brain Image Analysis: First International Workshop, MBIA 2011, Held in Conjunction with MIC-CAI 2011, Toronto, Canada, September 18, 2011. Proceedings 1.* 2011. Springer.
25. Hojjati SH, et al. Predicting conversion from MCI to AD using resting-state fMRI, graph theoretical approach and SVM. *J Neurosci Methods.* 2017;282:69–80.
26. Hirao K, et al. The prediction of rapid conversion to Alzheimer's disease in mild cognitive impairment using regional cerebral blood flow SPECT. *Neuroimage.* 2005;28(4):1014–21.
27. Margulies DS, et al. Situating the default-mode network along a principal gradient of macroscale cortical organization. *Proc Natl Acad Sci.* 2016;113(44):12574–9.
28. Bolt T, et al. A parsimonious description of global functional brain organization in three spatiotemporal patterns. *Nat Neurosci.* 2022;25(8):1093–103.
29. Park BY, et al. An expanding manifold in transmodal regions characterizes adolescent reconfiguration of structural connectome organization. *eLife.* 2021;10:e64694.
30. Park B-Y, et al. Differences in subcortico-cortical interactions identified from connectome and microcircuit models in autism. *Nat Commun.* 2021;12(1):2225.
31. Ottoy J, et al. Tau follows principal axes of functional and structural brain organization in Alzheimer's disease. *Nat Commun.* 2024;15(1):5031.
32. Weiner MW, et al. The Alzheimer's Disease Neuroimaging Initiative: a review of papers published since its inception. *Alzheimers Dement.* 2013;9(5):e111–94.
33. LaMontagne PJ, et al. OASIS-3: longitudinal neuroimaging, clinical, and cognitive dataset for normal aging and Alzheimer disease. *MedRxiv.* 2019;12:13.19014902.
34. Lee E, et al. BFLCRM: A Bayesian functional linear Cox regression model for predicting time to conversion to Alzheimer's disease. *The annals of applied statistics.* 2015;9(4):2153.
35. Sørensen A, et al. Prognosis of conversion of mild cognitive impairment to Alzheimer's dementia by voxel-wise Cox regression based on FDG PET data. *Neuroimage Clin.* 2019;21:101637.
36. Esteban O, et al. fMRIPrep: a robust preprocessing pipeline for functional MRI. *Nat Methods.* 2019;16(1):111–6.
37. Avants BB, Tustison N, Song G. Advanced normalization tools (ANTs). *Insight j.* 2009;2(365):1–35.
38. Fischl B. FreeSurfer. *Neuroimage.* 2012;62(2):774–81.
39. Pruim RH, et al. ICA-AROMA: A robust ICA-based strategy for removing motion artifacts from fMRI data. *Neuroimage.* 2015;112:267–77.
40. Kong D, et al. Predicting Alzheimer's disease using combined imaging-whole genome SNP data. *J Alzheimers Dis.* 2015;46(3):695–702.
41. Anderson-Bergman C. icenReg: regression models for interval censored data in R. *J Stat Softw.* 2017;81:1–23.
42. Schaefer A, et al. Local-global parcellation of the human cerebral cortex from intrinsic functional connectivity MRI. *Cereb Cortex.* 2018;28(9):3095–114.
43. Desikan RS, et al. An automated labeling system for subdividing the human cerebral cortex on MRI scans into gyral based regions of interest. *Neuroimage.* 2006;31(3):968–80.
44. Coifman RR, Lafon S. Diffusion maps. *Appl Comput Harmon Anal.* 2006;21(1):5–30.
45. Tenenbaum JB, Silva VD, Langford JC. A global geometric framework for nonlinear dimensionality reduction. *Science.* 2000;290(5500):2319–23.
46. Von Luxburg U. A tutorial on spectral clustering. *Stat Comput.* 2007;17:395–416.
47. Hong S-J, et al. Atypical functional connectome hierarchy in autism. *Nat Commun.* 2019;10(1):1022.
48. Van Essen DC, et al. The Human Connectome Project: a data acquisition perspective. *Neuroimage.* 2012;62(4):2222–31.
49. Kim S, et al. Comparison of different group-level templates in gradient-based multimodal connectivity analysis. *Network Neurosci.* 2024:1–49. https://direct.mit.edu/netn/article/doi/10.1162/netn_a_00382/120980/Comparison-of-different-group-level-templates-in.
50. Langs, G., P. Golland, and S.S. Ghosh. Predicting activation across individuals with resting-state functional connectivity based multi-atlas label fusion. in *Medical Image Computing and Computer-Assisted Intervention—MICCAI 2015: 18th International Conference, Munich, Germany, October 5–9, 2015, Proceedings, Part II 18.* 2015. Springer.
51. de Vos WR, et al. BrainSpace: a toolbox for the analysis of macroscale gradients in neuroimaging and connectomics datasets. *Commun Biol.* 2020;3(1):103.
52. Lee WJ, et al. Regional A β -tau interactions promote onset and acceleration of Alzheimer's disease tau spreading. *Neuron.* 2022;110(12):1932–1943.e5.
53. Verger A, et al. The pons as reference region for intensity normalization in semi-quantitative analysis of brain 18 FDG PET: application to metabolic changes related to ageing in conventional and digital control databases. *EJNMMI Res.* 2021;11:1–7.
54. Cox DR. Regression models and life-tables. *J Roy Stat Soc: Ser B (Methodol).* 1972;34(2):187–202.
55. Tibshirani R. Regression shrinkage and selection via the lasso. *J Roy Stat Soc: Ser B (Methodol).* 1996;58(1):267–88.
56. Hoerl AE, Kennard RW. Ridge regression: Biased estimation for non-orthogonal problems. *Technometrics.* 1970;12(1):55–67.
57. Zou H, Hastie T. Regularization and variable selection via the elastic net. *J Royal Stat Soc: Series B (statistical methodology).* 2005;67(2):301–20.
58. Simon N, et al. Regularization paths for Cox's proportional hazards model via coordinate descent. *J Stat Softw.* 2011;39(5):1.
59. Haak KV, Beckmann CF. Understanding brain organisation in the face of functional heterogeneity and functional multiplicity. *Neuroimage.* 2020;220: 117061.
60. Huntenburg JM, Bazin P-L, Margulies DS. Large-scale gradients in human cortical organization. *Trends Cogn Sci.* 2018;22(1):21–31.
61. Yeo BT et al. The organization of the human cerebral cortex estimated by intrinsic functional connectivity. *J Neurophysiol.* 2011;106(3):1125–65.
62. Mesulam MM. From sensation to cognition. *Brain: J Neurol.* 1998;121(6):1013–52.
63. Melrose RJ, et al. The neural correlates of naming and fluency deficits in Alzheimer's disease: an FDG-PET study. *International Journal of Geriatric Psychiatry: A journal of the psychiatry of late life and allied sciences.* 2009;24(8):885–93.
64. Golby A, et al. Memory encoding in Alzheimer's disease: an fMRI study of explicit and implicit memory. *Brain.* 2005;128(4):773–87.
65. Gomar JJ, et al. Increased retention of tau PET ligand [18F]-AV1451 in Alzheimer's Disease Psychosis. *Transl Psychiatry.* 2022;12(1):82.
66. Tekin S, Cummings JL. Frontal-subcortical neuronal circuits and clinical neuropsychiatry: an update. *J Psychosom Res.* 2002;53(2):647–54.
67. Sampath D, Sathyanesan M, Newton SS. Cognitive dysfunction in major depression and Alzheimer's disease is associated with hippocampal-prefrontal cortex dysconnectivity. *Neuropsych Dis Treat.* 2017;13:1509–19.
68. Stark SM, et al. Modulation of associative learning in the hippocampal-striatal circuit based on item-set similarity. *Cortex.* 2018;109:60–73.
69. Albouy G, et al. Both the hippocampus and striatum are involved in consolidation of motor sequence memory. *Neuron.* 2008;58(2):261–72.
70. Packard MG, Teather LA. Amygdala modulation of multiple memory systems: hippocampus and caudate-putamen. *Neurobiol Learn Mem.* 1998;69(2):163–203.
71. Calabro FJ, et al. Development of hippocampal–prefrontal cortex interactions through adolescence. *Cereb Cortex.* 2020;30(3):1548–58.
72. O'Callaghan C, et al. Hippocampal atrophy and intrinsic brain network dysfunction relate to alterations in mind wandering in neurodegeneration. *Proc Natl Acad Sci.* 2019;116(8):3316–21.

73. Ossenkoppele R, et al. Amyloid and tau PET-positive cognitively unimpaired individuals are at high risk for future cognitive decline. *Nat Med*. 2022;28(11):2381–7.
74. Biel D, et al. Tau-PET and in vivo Braak-staging as prognostic markers of future cognitive decline in cognitively normal to demented individuals. *Alzheimer's Res Ther*. 2021;13(1):137.
75. Sperling RA, et al. The impact of amyloid-beta and tau on prospective cognitive decline in older individuals. *Ann Neurol*. 2019;85(2):181–93.
76. Langbaum JB, et al. Categorical and correlational analyses of baseline fluorodeoxyglucose positron emission tomography images from the Alzheimer's Disease Neuroimaging Initiative (ADNI). *Neuroimage*. 2009;45(4):1107–16.
77. Nestor PJ, et al. Limbic hypometabolism in Alzheimer's disease and mild cognitive impairment. *Ann Neurol*. 2003;54(3):343–51.
78. Mosconi L, et al. Reduced hippocampal metabolism in MCI and AD: automated FDG-PET image analysis. *Neurol*. 2005;64(11):1860–7.
79. Mosconi L, et al. Multicenter standardized 18F-FDG PET diagnosis of mild cognitive impairment, Alzheimer's disease, and other dementias. *J Nucl Med*. 2008;49(3):390–8.
80. Anchisi D, et al. Heterogeneity of brain glucose metabolism in mild cognitive impairment and clinical progression to Alzheimer disease. *Arch Neurol*. 2005;62(11):1728–33.
81. Mosconi L, et al. MCI conversion to dementia and the APOE genotype: a prediction study with FDG-PET. *Neurol*. 2004;63(12):2332–40.
82. Wessels AM, Dowsett S, Sims J. Detecting Treatment Group Differences in Alzheimer's disease clinical trials: a comparison of alzheimer's disease assessment scale-Cognitive Subscale (ADAS-Cog) and the Clinical Dementia Rating-Sum of Boxes (CDR-SB). *J Prevent Alzheimer's Dis*. 2018;5:15–20.

Publisher's Note

Springer Nature remains neutral with regard to jurisdictional claims in published maps and institutional affiliations.